

Optimal Design and Noise Analysis of High-Performance DBR-Integrated Lateral Germanium (Ge) Photodetectors for SWIR Applications

Harshvardhan Kumar (✉ harshvardhan.kumar@lnmiit.ac.in)

The LNM Institute of Information Technology

Ankit Kumar Pandey

Bennett University, Greater Noida

Chu-Hsuan Lin

National Dong Hwa University

Research Article

Keywords: Optimal Design, Noise Analysis, Lateral Germanium

Posted Date: November 15th, 2021

DOI: <https://doi.org/10.21203/rs.3.rs-1054935/v1>

License:  This work is licensed under a Creative Commons Attribution 4.0 International License.

[Read Full License](#)

Optimal Design and Noise Analysis of High-Performance DBR-Integrated Lateral Germanium (Ge) Photodetectors for SWIR Applications

Harshvardhan Kumar^{1,*}, Ankit Kumar Pandey², and Chu-Hsuan Lin^{3,*}

¹The LNM Institute of Information Technology, Department of Electronics and Communication Engineering, Jaipur, 302031, India

²Bennett University, Department of Electronics and Communication Engineering, Greater Noida, 201310, India

³National Dong Hwa University, Department of Opto-Electronic Engineering, Hualien, 974301, Taiwan

*harshvardhan.kumar@lnmiit.ac.in (H.K.); chlin0109@gms.ndhu.edu.tw (C.H.L.)

Abstract

This work presents the high-performance Si/SiO₂ distributed Bragg reflector (DBR)-integrated lateral germanium (Ge) *p-i-n* photodetectors (PDs) for atmospheric gas sensing and fiber-optic telecommunication networks in the short-wave infrared (SWIR) regime. In addition, this study also proposes an opto-electronic compact small-signal noise equivalent circuit model (SSNECM) of the designed device to compute the signal-to-noise ratio (SNR) at the output of the detector. Various figure-of merits including current under dark and illumination, responsivity, detectivity, 3dB bandwidth, and the SNR of the proposed device are estimated at the room-temperature (RT) for an incident optical power of 0.5 μW . Furthermore, the impact of scaling of rib waveguide (WG) width and height on dark current, responsivity, and 3dB bandwidth are investigated to optimize the proposed device. The validation of the proposed model is done by comparing various parameters including dark current, responsivity, and detectivity of the designed device with other Ge PDs. The estimated results show the reduced *trade-off* between responsivity and 3dB bandwidth of the designed device. At $\lambda = 1550$ nm, the proposed device achieves the high detectivity and SNR of $> 2 \times 10^{11}$ Jones and 120 dB (up to 3 THz), respectively, with the bias voltage of -2V. These encouraging results pave the path for the future development of low noise and high-speed detectors for SWIR applications.

Introduction

The detection of short-wave infrared (SWIR, 1 – 1.7 μm) wavelengths has significant applications including fiber-optic telecommunication¹, optical gas sensing², civilian and military applications³, biosensors⁴, night vision⁵, and health monitoring systems^{6,7}. SWIR detection requires high-responsivity photodetectors (PDs) with high speed and low noise. Traditionally, mercury cadmium tellurium (HgCdTe) and InGaAs-based PDs are used for SWIR wavelength detection^{8–11}. These PDs are very sensitive and robust. However, they require a complex fabrication process and high cost as well. In addition, HgCdTe and InGaAs contain heavy metals such as Hg and highly toxic materials such as Cd and As, which are dangerous for human beings¹². Moreover, they are incompatible with silicon technology. On the other hand, Si-based PDs have been extensively used in the near-infrared (NIR) spectral range due to their matured technology and low cost^{13,14}. However, its relatively large bandgap energy of 1.12 eV limits the absorption cutoff (λ_c) of 1.1 μm . As a result, Si-based PDs are not suitable for SWIR wavelength detection. Fortunately, germanium (Ge) is one of the most promising group-IV material for SWIR wavelength detection owing to its small direct bandgap of 0.8 eV at room temperature and fully compatible with Si complementary metal-oxide-semiconductor (CMOS) technology^{15,16}. Therefore, it is highly desirable to develop high-responsivity Ge-based PDs with high-speed at the SWIR bands.

Over the last few decades, several metal-semiconductor-metal (MSM) and *p-i-n* type Ge PDs have been extensively studied^{17–23}. Usually, the dark current of *p-i-n* PDs is relatively smaller than the MSM PDs because of the on/off characteristics of the *p-n* junction²⁴. Recently, Ge PDs on Ge-on-insulator (GOI) platform have been studied for further reduction in dark current, owing to the reduced defect density^{23,25–28}. In addition, in recent years, several techniques such as waveguide and resonant-cavity-enhanced (RCE) structures have been invented to improve the spectral responsivity (SR) of *p-i-n* Ge PDs^{29–33}. Among those techniques, RCE PDs can be a promising device to reduce the *trade-off* between 3dB bandwidth (f_{3dB}) and spectral responsivity. Thus, RCE PDs can achieve high f_{3dB} and SR simultaneously at a particular wavelength. Furthermore, the greatest advantage of using the RCE technique in optical communication networks is its excellent wavelength selectivity for dense wavelength division multiplexing (DWDM) to get the enhanced data transport capacity.

In recent decades, a few works on vertical *p-i-n* PDs on silicon-on-insulator (SOI) substrate have been reported^{34–}

³⁶. The SR of their devices at 1550 nm were 0.18 A/W³⁴, 0.842 A/W³⁵, and 0.249 A/W³⁶, on the other hand, their 3dB bandwidth was 9.7 GHz³⁴, 19 GHz³⁵, and 20.6 GHz³⁶ on SOI substrate. These encouraging results show that RCE Ge *p-i-n* PDs can be a promising detector for the SWIR regime. The responsivity and 3dB bandwidth of the device can be further improved by the integration of high-quality (Q) factor distributed Bragg reflector (DBR) and lateral Ge *p-i-n* PDs. To the best of the authors' knowledge, there is no DBR-integrated lateral Ge PDs have been reported yet, thus hindering the development of high-performance SWIR Ge PDs. Therefore, it is interesting to study and predict the performance of DBR-integrated lateral Ge *p-i-n* PDs.

Here, we propose a novel DBR (Si/SiO₂: n_H/n_L)-integrated lateral Ge *p-i-n* PDs on Si substrate to get high-speed and high responsivity, simultaneously. The Si/SiO₂(n_H/n_L) DBR was used to reflect the transmission light for the enhancement of light-matter interaction and thus, finally photo-generated carrier collection efficiency. Furthermore, in this work, lateral Ge PDs on the Si platform were considered to meet the requirements of electronic-photonic integrated circuits (EPICs). In addition, our designed lateral Ge PDs structure provides the better decoupling of photon absorption and photon generated carrier path which reduces the *trade-off* between the responsivity and 3dB bandwidth of the device. Our lateral Ge *p-i-n* homojunction also enhances the optical confinement factor (OCF) in the intrinsic Ge layer, thereby, increasing the optical responsivity. The performance of the designed device was studied via electrical and optical simulation in the SWIR regime (1200 to 1600 nm) using COMSOL Multiphysics and MATLAB software. The impact of scaling of rib waveguide width and height was also studied to get the optimal performance of the proposed device. Furthermore, to the best of our knowledge, we present for the first time the small-signal noise equivalent circuit model (SSNECM) of lateral Ge *p-i-n* PDs. The analytical expressions for the transfer function and signal-to-noise ratio (SNR) were also derived based on the presented SSNECM. The proposed SSNECM examined several light interactions happening inside the device such as the junction and parasitic capacitances, and resistances. The presented SSNECM consists of various noise components including shot noise current source and thermal noise current source to characterize the noise performance. The results revealed that the proposed circuit model accurately examined the noise present and the SNR of the device in the high-frequency operation. Therefore, it can be useful for noise characterization and high-performance circuit designing.

Device Structure and Optical Characterization

The proposed device structure is shown in Fig. 1(a) in which layers are grown pseudomorphically on the Si substrate. From fabrication point of view, the Si/SiO₂ DBR structure can be formed by transfer printing technique³⁷. The top Si layer and active Ge regions are intrinsic. Doping concentration of the p-type Si buffer layer (400 nm) is 10¹⁶ cm⁻³. The structure is coated with SiO₂ for minimizing the light reflection. Light (0.5 μW) is made to the incident on the top of the structure. The top SiO₂ antireflection (AR) coating form a high Q-factor resonant cavity with the bottom DBR structure. Each DBR pair is having a thickness of 330 nm (Si: 100 nm; SiO₂: 230 nm). The presented DBR pair thickness is chosen using the relation $\lambda/4n$, where λ and n are the incident light wavelength and refractive index, respectively. High reflectivity is experienced in the DBR structure as indicated in Fig 1(b). This reflectivity enhances the light-matter interaction in the active region. The interaction results in peak responsivity at a particular wavelength. Thus, wavelength selectivity is an additional advantage of using DBR structure apart from high responsivity behavior.

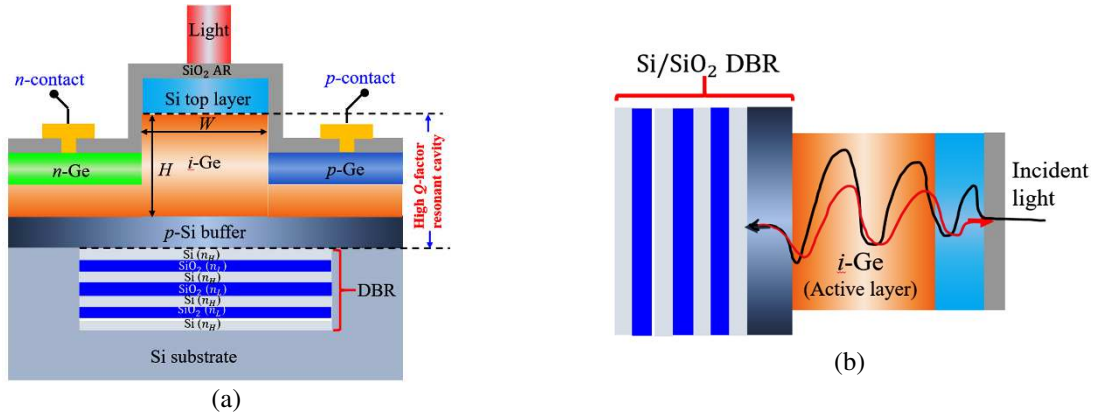


Fig. 1 (a) Two-dimensional (2-D) Si/SiO₂ DBR-integrated lateral Ge *p-i-n* homojunction PD on Si substrate and (b) Pattern of reflectivity in the active layer caused by the DBR pairs.

The optimal range of aspect ratio of rib waveguide can be determined using the expression as follows³⁸;

$$\frac{W}{H} \leq \alpha + \frac{r}{\sqrt{1-r^2}}; \text{ for } 0.5 \leq r \leq 1.0 \quad (1)$$

where, W/H is the aspect ratio of rib waveguide width to the height, r is the slab height to the total height of rib waveguide. The value of $\alpha = 0.3$ is considered in this work.

Initially, the guiding mode of the designed waveguide structure is analyzed in order to evaluate the optical confinement. The finite element method (FEM) simulated quasi-TE fundamental mode along with the normalized optical confinement factor (OCF) for the waveguide structure is shown in Fig. 2(a). The structure width of $5 \mu\text{m}$ (5-pairs of DBR) is considered with the incident light wavelength of 1310 nm . Here the top Si and the bottom DBR pairs (Si/SiO₂) provide good optical confinement for the Ge active layer which facilitates proper light confinement in the rib structure for a small aspect ratio of 1.3. As a result, a good optical confinement factor larger than 95% can be achieved, which is significantly sensitive to the DBR pairs. These figures (Fig. 2(a)) show different quasi-TE modes for the waveguide structure based on different eigenfrequency values. Along the vertical direction, only one mode is seen because the thickness is less than a half of the wavelength. Further, along the horizontal direction, although the structure can support many modes, the overlap of the guiding mode with the intrinsic Ge active layer can maintain high, so the OCF can also be greater than 95%. Additionally, Fig. 2(b) shows the variation of OCF increment (in percentage) with the number of DBR pairs in the case of two incident wavelengths. The variation is similar for both cases. This high OCF directs towards the high responsivity applicability of the proposed PD in the SWIR region especially at 1330 and 1550 nm .

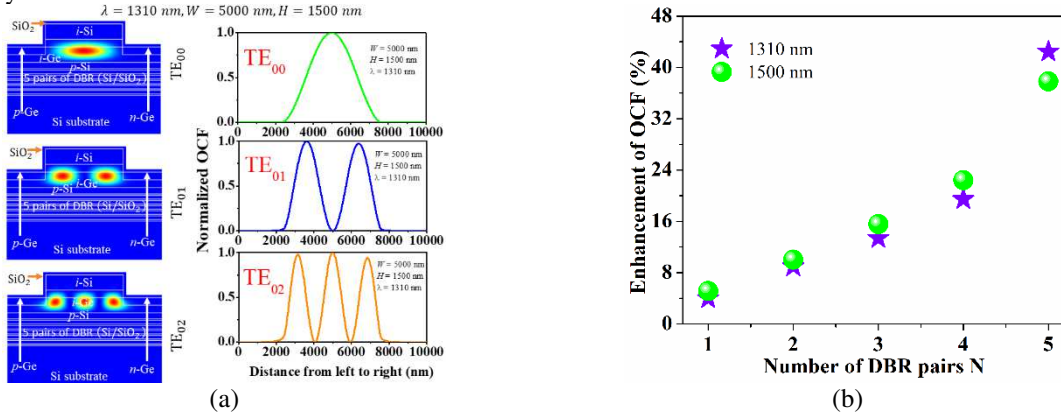


Fig. 2 (a) FEM simulated quasi-TE fundamental mode along with the normalized optical confinement factor (OCF) for the waveguide structure and (b) Variation of OCF increment (in percentage) with the number of DBR pairs in the case of two incident wavelengths.

Results and Discussion

Dark and illumination I-V characteristics. Si/SiO₂ DBR integrated lateral Ge homojunction $p-i-n$ PDs were characterized by simulating I-V curves under dark and illuminated conditions.

Fig. 3a shows typical I-V characteristics of the designed device simulated at room temperature (RT) and shows the excellent rectification characteristics of lateral $p-i-n$ homojunction. Under a reverse bias voltage of -2V , the device exhibits a dark current of $\sim 0.54 \text{ pA}$ at RT for $W = 4000 \text{ nm}$, as shown in Fig. 3a. To the best of the authors' knowledge, it is the lowest value than those of other Ge PDs on Si and SOI substrates^{31,32,34-36,39}. Theoretically, the rectification behavior of $p-i-n$ diode can be analyzed using the equation⁴⁰;

$$I_{dark} = I_0 \times \exp \left[\frac{q(V_{bias} - R_s I_{net})}{\eta k T} \right] + \frac{V_{bias}}{R_{shunt}} \quad (2)$$

where, I_0 and η are the reverse saturation current and ideality factor, respectively. q , k , and T are the charge of an electron, Boltzmann constant, and temperature in Kelvin. I_{net} is the net current flowing through the diode in forward bias condition under dark condition, which can be calculated using, $I_{net} = I_{dark} - (V_{bias}/R_{shunt})$. R_s and R_{shunt} are the series and shunt resistances, respectively, calculated under forward bias and reverse bias. R_{shunt} can be calculated by taking the first derivative of I-V near zero voltage, $R_{shunt} = \left(\frac{dI}{dV} \right)^{-1}$. Ideally, infinite shunt resistance is desired to eliminate the thermal noise. The series resistance can be calculated from both the simulated and measured I-V curve in forward bias using the expressions;

$$R_s = \frac{dV_{bias}}{dI_{net}} - \frac{\eta k T}{q I_{net}} \quad (3)$$

The calculated values of R_{shunt} and R_s from the simulated I-V characteristics are $236.7 \text{ G}\Omega$ and 0.5Ω , respectively for $W = 4000 \text{ nm}$. The low series resistance and high shunt resistance obtained here suggest a good Ohmic contact

of the device and indicate a low leakage current. In addition, to further understand the behavior of dark current, I-V curves were also calculated for different rib waveguide widths, as shown in the inset of Fig. 3a. The obtained results show an increase of I_{dark} under reverse bias and a decrease of I_{dark} under forward bias with increasing rib waveguide width. Principally, I_{dark} consists of two major components: surface leakage current (I_{surf}) and the bulk leakage current (I_{bulk}). Generally, I_{surf} contributes significantly to I_{dark} than I_{bulk} . The reason is attributed to the generation of minority carriers at the surface states on Ge layer sidewalls mainly governed by the Shockley-Read-Hall (SRH) recombination process.

Fig. 3b shows the I-V curve under the illumination of $0.5 \mu W$ at 1310 nm . The photogenerated current (I_{ph}) simulated under the reverse bias voltage is higher with at least five orders of magnitude compared with I_{dark} , proving that the Ge-based films are highly photosensitive. The similar-gains were also reported in the literature for different Ge-based films³⁵, which confirms the validity of the obtained results in this work.

The validation of the proposed model was also done by comparing the I-V characteristics of the designed device with lateral *p-i-n* silicon-germanium-silicon (Si-Ge-Si) heterojunction PD²², the result is shown in Fig. 3c. The cross-sectional area of the waveguide in both devices is the same ($\sim 6 \mu m^2$) so that a relevant comparison is possible. Fig. 3c depicts the dark current of both the devices under applied reverse bias. As noticed, the proposed device exhibits lower I_{dark} at least five orders of magnitude compared with Si-Ge-Si PD because of the reduced tunneling current at the homojunction and lower leakage current. In addition, for the proposed device, the dark current is almost constant throughout the applied reverse bias, resulting in a high shunt resistance. However, a significant increment of I_{dark} for applied reverse bias can be observed for Si-Ge-Si PD, which results in lower shunt resistance. As a result, the thermal noise of Si-Ge-Si *p-i-n* PD will be higher than the designed device. Therefore, this significant comparison confirms that the designed device can perform better than earlier reported Ge PDs.

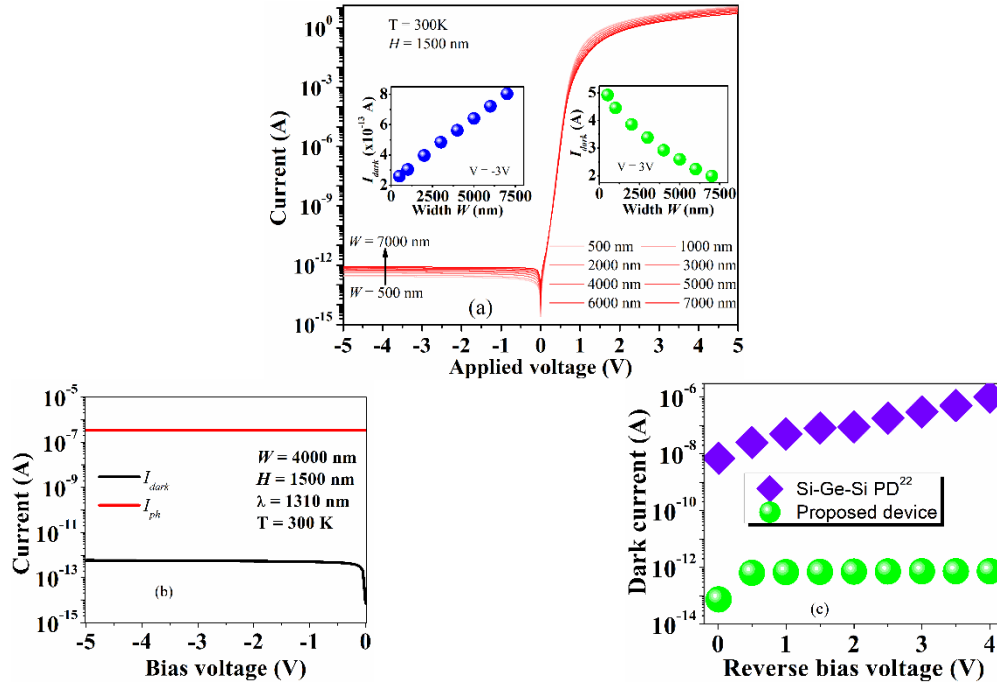


Fig.3 (a) Dark current with different rib waveguide width as a function of bias voltage at room-temperature. The inset shows the variation of dark current under reverse bias and forward bias with varying width. (b) Variation of current under dark and illumination at $\lambda = 1310 \text{ nm}$ with incident optical power of $0.5 \mu W$, and (c) Comparative I-V characteristics of the designed device with lateral *p-i-n* silicon-germanium-silicon (Si-Ge-Si) heterojunction PD²².

Optical properties and the effect of aspect ratio on the photoresponse. The variation of the absorption coefficient (α) with wavelength (λ) for Ge film at RT, considering the absorption bands of various gases such as O_2 at 1270 nm , H_2O at 1380 nm , and CO_2 at 1400 nm , and fiber-optic telecommunication bands at 1310 nm and 1550 nm , respectively is shown in Fig.4. The absorption coefficient of Ge film was calculated using the expression⁴¹. An estimation of bandgap energy (E_g) of Ge film can also be made from the absorption coefficient spectrum (Fig. 4). The corresponding direct bandgap energy of Ge film is 0.7985 eV at RT.

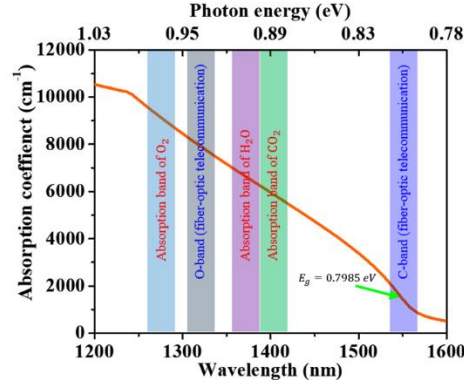


Fig. 4 Calculated absorption spectra for pseudomorphic Ge at $T = 300\text{ K}$.

Next, the photoresponse specifically in terms of spectral responsivity of Si/SiO₂ DBR integrated lateral Ge homojunction *p-i-n* PDs were simulated in the spectral range of 1200 nm to 1600 nm. The prime objective of selecting this broad spectral range was to cover the absorption edges of various atmospheric gases such as O₂, H₂O, and CO₂ and fiber-optic telecommunication bands. In addition, the reflectivity of Si/SiO₂ DBR is ~100% and constant throughout this selected wavelength spectrum. As a result, light-matter interaction will be maximum in the active region. Theoretically, the responsivity of a PD can be calculated as;

$$R(\lambda) = \frac{I_{ph}(\lambda)}{P_{in}} \quad (4)$$

where, $I_{ph}(\lambda)$ is the wavelength-dependent photogenerated current under illumination and P_{in} is the incident optical power. Fig. 5 shows the spectral responsivity (SR) of the designed device with varying rib waveguide width, height and their corresponding aspect ratio at a bias voltage of -2V. Fig. 5a shows the evolution of SR of the designed device as a function of increasing width for sensing various atmospheric gases at 1270 nm, 1380 nm, and 1400 nm, respectively for a fixed height of rib waveguide ~1500 nm. The responsivity decreases with increasing waveguide width. The reason may be attributed to the increased adverse losses at the selected wavelengths. The calculated result reveals that a narrower rib waveguide width is suggested to get the highest SR at the above-selected wavelengths for sensing atmospheric gases. Next, to get the optimal width and height for sensing applications, the SR of the device was also calculated with the varying height of rib waveguide for a fixed waveguide width of 1000 nm at -2V. The simulated result suggested that the preferable height of the rib waveguide should be 1300 nm to get the highest responsivity. Therefore, based on the simulated results, the reasonable width and height of 1000 nm and 1300 nm were chosen in this work to optimize the aspect ratio (W/H) in order to get the highest responsivity for sensing atmospheric gases at 1270 nm, 1380 nm, and 1400 nm, respectively. For the optimal width and height, the spectral responsivities of the device are 542.3 mA/W, 642.7 mA/W, and 832.04 mA/W at wavelengths of 1270 nm, 1380 nm, and 1400 nm, respectively.

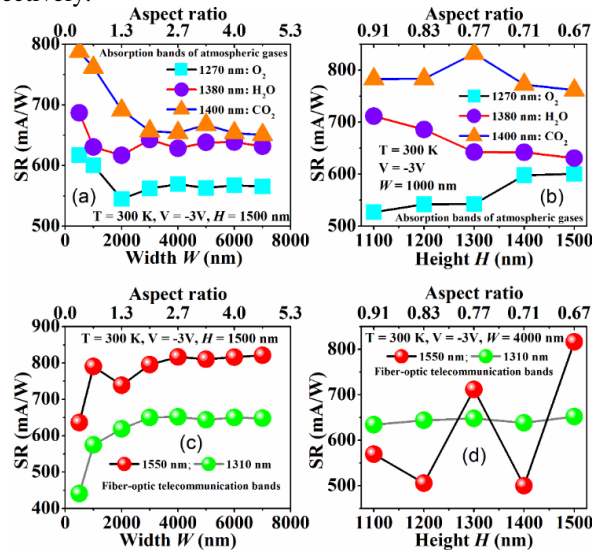


Fig. 5 Simulated spectral responsivity as a function of aspect ratio, rib waveguide width, and height for the proposed device at $T = 300\text{ K}$.

Similarly, to get the optimal aspect ratio at fiber-optic telecommunication bands, the spectral responsivity was calculated with varying width and height, results are shown in Fig. 5c and 5d. For $500 \text{ nm} \leq W \leq 4000 \text{ nm}$, spectral responsivity increases but it tends to be saturated for $W \geq 4000 \text{ nm}$. The reason for the enhanced responsivity with increasing width is attributed to the increased absorption of the device. However, the variation of height has no significant impact on the spectral responsivity at 1310 nm but it has a noticeable impact on the responsivity at 1550 nm . The reason for this behavior may be attributed to the resonance effect caused by the vertical resonant cavity. The simulated results suggest the optimal width and height of 4000 nm and 1500 nm to get the highest responsivities of 652.08 mA/W and 816.55 mA/W at wavelengths of 1310 nm and 1550 nm , respectively.

Next, the bias-dependent responsivity of the proposed device at 1550 nm was also calculated and compared with values obtained for lateral Si-Ge-Si heterojunction PD²², the result is presented in Fig. 6. The cross-sectional area of the waveguide in both the device was kept the same ($\sim 6 \mu\text{m}^2$) to make a meaningful comparison. The spectral responsivity of the designed device is less dependent on the applied bias voltage because of the high electric field ($> 10^6 \text{ V/m}$) and nearly constant within the intrinsic Ge region for the applied bias voltage. However, the significant increase in spectral responsivity of Si-Ge-Si PD with applied bias voltage can be observed. This is due to an increase of electric field within the intrinsic Ge region with applied bias voltage. This comparison reveals that Si/SiO₂ DBR integrated lateral Ge homojunction *p-i-n* PD achieved $\sim 308.2\%$ higher responsivity than the value of responsivity obtained for Si-Ge-Si heterojunction PD²².

In addition, the encouraging responsivity curve of Si/SiO₂ DBR integrated lateral Ge homojunction *p-i-n* PD indicates that the device can yield very high external quantum efficiency (EQE), approaching the theoretical limit of $\sim 100\%$. Particularly, DBR integrated lateral Ge *p-i-n* homojunction PD transform very efficiently the incident photon into electrons and thus photogenerated current. The EQE of PD can be calculated as follows:

$$EQE = \frac{1240 \times R(\lambda)}{\lambda \text{ (nm)}} \quad (5)$$

where, $R(\lambda)$ is the wavelength-dependent responsivity and $\lambda \text{ (nm)}$ is the wavelength in nm . Similar to the spectral responsivity of the device, EQE shows the same trends with the varying width and height of the rib waveguide. At -2 V and 1550 nm operating wavelength, EQE of the proposed device is equal to $\sim 65.3\%$ for the cross-sectional area of waveguide $\sim 6 \mu\text{m}^2$, which is almost 4.7 times higher than the value obtained for Si-Ge-Si PD²² for having the same cross-sectional area.

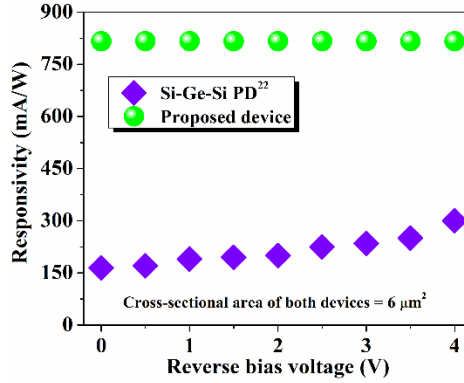


Fig. 6 Comparison of bias-dependent spectral responsivity of the proposed device with lateral Si-Ge-Si heterojunction PD²² at $\lambda = 1550 \text{ nm}$.

Analysis of specific detectivity of designed device. Apart from the calculation of spectral responsivity, the performance of PDs can also be characterized by specific detectivity (D^*). Generally, it represents the potentiality of a PD to detect weak incident light signals. Detectivity and responsivity of any PD are directly related to each other according to the following mathematical expression⁴²:

$$D^* = \frac{R(\lambda) \times \sqrt{A \Delta f}}{i_n} = \frac{R(\lambda) \times \sqrt{A \Delta f}}{\sqrt{I_{shot}^2 + I_{th}^2}} \quad (6)$$

where, A is the photosensitive area. Δf is the bandwidth, which is usually considered as 1 Hz ⁴³. I_{shot} is the shot noise current mainly due to current under dark and illumination and I_{th} is the Johnson noise due to the thermal vibrations of carriers. I_{shot} and I_{th} can be calculated using the equations as follows:

$$I_{shot} = \sqrt{2q(I_{dark} + I_{ph})\Delta f} \quad (7)$$

$$I_{th} = \sqrt{\frac{4kT\Delta f}{R_{shunt}}} \quad (8)$$

where, R_{shunt} is the shunt resistance. It can be concluded from equation (6) that low dark current, high responsivity, and high shunt resistance are desired for any PD to manifest high detectivity. Fig. 7 shows the estimated detectivity of the designed device as a function of reverse bias voltage at RT. The peak detectivity of the simulated Si/SiO₂ DBR integrated lateral Ge homojunction *p-i-n* PD is predicted to be $\sim 2.4 \times 10^{11}$ Jones for $W = 4000$ nm and $H = 1500$ nm at $\lambda = 1550$ nm and -2V. Here, the high detectivity reveals that the designed device is highly sensitive to the weak optical signal. The reason for this high detectivity is attributed to the reduced I_{shot} and I_{th} because of the lower I_{dark} and higher R_{shunt} for the designed device. The order of specific detectivity estimated in this work is significantly higher as compared to other reported Ge-based PDs⁴⁴. The estimated detectivity is also two orders of magnitude higher than the commercial Ge PD⁴⁵ developed on defect-free bulk Ge and As-200 and control GOI devices⁴³, a comparison is also shown in the inset of Fig. 7. Most importantly, the designed device exhibits high detectivity at small reverse bias voltage, which makes the device low power consumption.

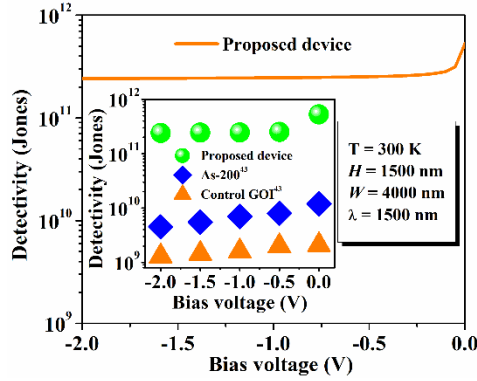


Fig. 7 Calculated detectivity of the device as a function of applied reverse bias at $T = 300$ K. The inset shows the comparison of detectivity of the proposed device with As-200 and Control GOI devices⁴³.

Analysis of opto-electrical frequency response. The opto-electrical frequency response of PDs has been investigated through the calculation of (i) 3dB bandwidth and (ii) the quantum-efficiency bandwidth product. The 3dB bandwidth of PD can be estimated using the equation as follows:

$$f_{3dB} = \sqrt{\frac{1}{\frac{1}{f_{trans}^2} + \frac{1}{f_{RC}^2}}} \quad (9)$$

where, f_{trans} is the carrier transit-limited bandwidth, which can be calculated as; $f_{trans} = 0.45v_{sat}/W$ and f_{RC} is the RC delay-limited bandwidth, which can be calculated as $f_{RC} = 1/(2\pi R_L C_j)$. v_{sat} represents the saturation drift velocity of the carrier (6×10^4 m/s) in Ge and R_L is the load resistance (50Ω) frequently used in network analyzers. C_j is the junction capacitance due to *p* – and *n* –doped Ge and can be calculated as; $C_j = \epsilon_0 \epsilon_r A_j / W$, where ϵ_r is the relative permittivity (16.2) of Ge, A_j is the junction area of the device, and W is the width of the intrinsic region (here the width of rib waveguide). Fig. 8 shows the calculated junction capacitance as the functions of waveguide width and the device length. Junction capacitance is significantly dependent on both the waveguide width and the device length. As the waveguide width increases, C_j decreases rapidly, however, it increases with the increasing the device length because of the increased cross-sectional area. Next, the calculated bandwidth of the device with a fixed device length of $1 \mu\text{m}$ as a function of increasing waveguide width is presented in Fig. 9(a). The calculated result shows that f_{trans} decreases with the increasing width because the photogenerated carriers have to travel a longer path. On the contrary, f_{RC} increases because of the decreasing behavior of junction capacitance with the width. This study reveals that f_{3dB} of the designed device is significantly dominated by f_{trans} . Fig. 9(b) demonstrates the calculated f_{3dB} of the proposed PDs as a function of rib waveguide width with different device lengths. The result indicates that f_{3dB} is strongly dependent on the device length for narrower width ($W < 1000$ nm) and less dependent for $W \geq 1000$ nm. However, it decreases steeply with increasing width because of the carrier transit-limited bandwidth. With optimal width of 1000 nm and 4000 nm and device length of $1 \mu\text{m}$ for atmospheric gas sensing and fiber-optic telecommunication applications, f_{3dB} of the designed device are 26.4 GHz and 6.6 GHz, respectively. This estimated high f_{3dB} indicates the high-speed operation of the proposed device. In addition, the quantum-efficiency bandwidth product with optimal width of 1000 nm for sensing various atmospheric gases at 1270 nm(O₂), 1380 nm(H₂O), and 1400 nm(CO₂) are

~14.1 GHz, ~15.4 GHz, and ~19.6 GHz, respectively. On the other hand, for fiber-optical telecommunication bands at 1310 nm and 1550 nm, the quantum-efficiency bandwidth product are ~4.1 GHz and ~4.3 GHz, respectively with the optimal width of 4000 nm. This quantum-efficiency bandwidth product is very crucial for the PDs design in terms of opto-electrical performance and footprint.

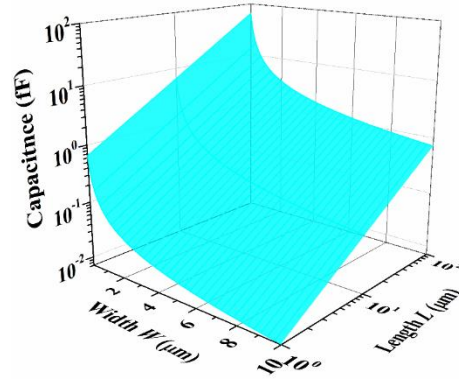


Fig. 8 Variation of calculated junction capacitance with rib waveguide width and length of the device.

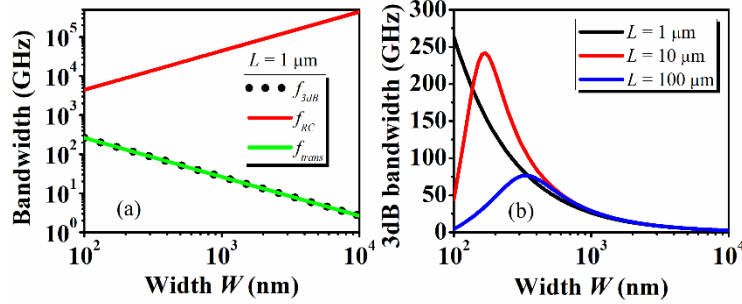


Fig. 9 (a) Variation of calculated bandwidth of the device as a function of width with fixed device length of $1\mu\text{m}$ and (b) 3dB bandwidth of the device as a function of width with different device lengths.

Small-signal noise equivalent circuit modeling (SSNECM) and signal-to-noise ratio (SNR) analysis.

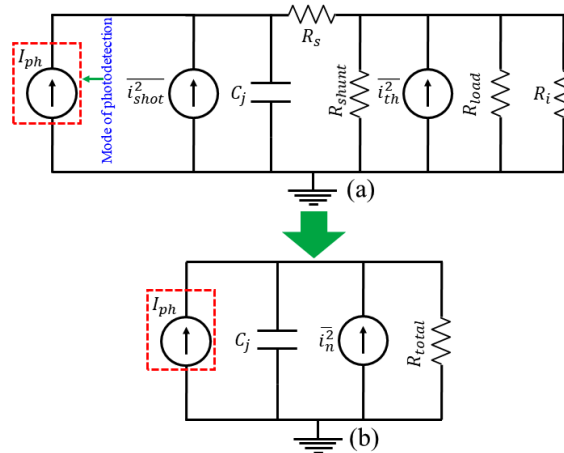


Fig. 10 (a) Proposed small-signal noise equivalent circuit model of the designed device and (b) simplified noise equivalent circuit model of the proposed small-signal noise equivalent circuit model of the device.

Fig. 10(a) presents the π – model SSNECM of the DBR-integrated lateral Ge p - i - n homojunction PDs with significant changes in the conventional small-signal circuit model of p - i - n diode. Fig. 10(b) shows the simplified equivalent circuit model of SSNECM (as shown in Fig. 10(a)). The proposed SSNECM consists of two major noise sources present in the p - i - n PD: shot noise (i_{shot}^2) and Johnson noise (i_{th}^2) and the mode of photodetection to detect optical

signals. However, the conventional small-signal circuit model of p - i - n diode doesn't comprise any noise source and the photodetection mode to detect optical signal. The magnitude of the shot noise source strongly depends on the dark current and photocurrent. On the other hand, thermal noise is significantly affected by the shunt resistance ($I_{th} \propto 1/\sqrt{R_{shunt}}$). Therefore, low dark current and high shunt resistance are strongly desired for the PDs to achieve high SNR.

Based on the presented SSNECM, the signal-to-noise ratio of PD can be computed by using the expression as follows:

$$SNR = \frac{i_{ph}^2 |H(s)|^2}{i_n^2(s)} \quad (10)$$

where, $i_n(s)$ and i_{ph} are the mean squared noise current source and photogenerated, respectively. $H(s)$ is the transfer function of the proposed SSNECM. The mean squared noise current source can be calculated as;

$$i_n^2(s) = i_{shot}^2 + i_{th}^2 = 2q(I_{dark} + I_{ph})\Delta f + \frac{4kT\Delta f}{R_{shunt}} \quad (11)$$

The transfer function of the proposed SSNECM can be expressed as;

$$H(s) = \frac{X_c}{R+X_c} = \frac{1/C_j s}{R_{total} + 1/C_j s} = \frac{1}{1 + R_{total} C_j s} \quad (12)$$

Where, s is the Laplace operator, taking $s = j\omega = j2\pi f$. R_{total} is the total resistance connected in the SSNECM and can be calculated as;

$$R_{total} = R_s + (R_{shunt} || R_{load} || R_i) \quad (13)$$

Where, R_i is the input impedance of the amplifier circuit, which is considered as $10 \text{ k}\Omega$ in this work.

Combining Eqs. 10 to 13, finally the expression to compute SNR of a PD can be given as;

$$SNR = i_{ph}^2 \times \left(\frac{1}{2q(I_{dark} + I_{ph})\Delta f + \frac{4kT\Delta f}{R_{shunt}}} \right) \times \left(\left| \frac{1}{1 + R_{total} C_j s} \right|^2 \right) \quad (14)$$

Fig. 11 (a) and (b) show the computed thermal and shot noise components (using Eq. 11) as a function of device operating frequency with optimal width and height of rib waveguide for an input impedance of $10 \text{ k}\Omega$ at RT. As shown in Fig. 11, all the noise sources are independent of frequency because they are white noise. The result reveals that device with $W = 4000 \text{ nm}$ and $H = 1500 \text{ nm}$ exhibits higher thermal noise compared to the device with $W = 1000 \text{ nm}$ and $H = 1300 \text{ nm}$ because of the reduced shunt resistance. In addition, the magnitude of the shot noise source is also higher for $W = 4000 \text{ nm}$ and $H = 1500 \text{ nm}$ than those of $W = 1000 \text{ nm}$ and $H = 1300 \text{ nm}$ because of the increased dark current.

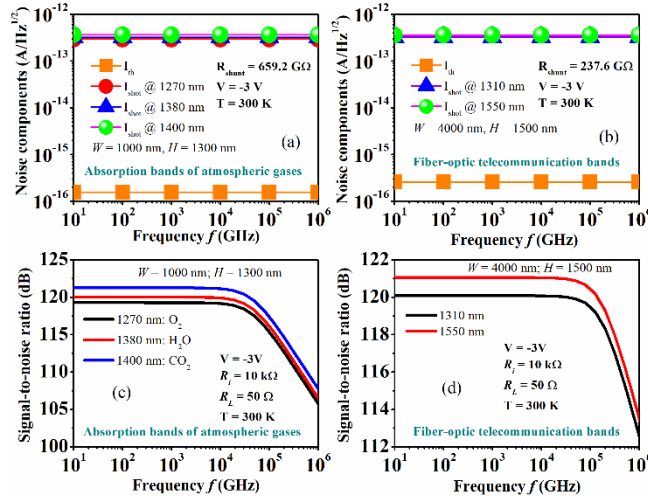


Fig. 11 Variation of various noise components at (a) absorption bands of atmospheric gases (b) fiber-optic telecommunication bands with operating frequency. Computed signal-to-noise ratio at (a) absorption bands of atmospheric gases (b) fiber-optic telecommunication bands with operating frequency at $T = 300 \text{ K}$.

Fig. 11 also suggests that thermal noise is independent of incident light wavelength. Conversely, shot noise is significantly dependent on the incident light wavelength because of the wavelength-dependent photocurrent. Most importantly, the order of thermal noise found in this work is three orders lower than compared to As-200 and Control GOI devices⁴³, which again confirms the potentiality of the proposed device. Next, the SNR at the output of PDs was also computed based on the calculated noise components. Fig. 11 (c) and (d) show the computed SNR as a function of operating frequency with different incident light wavelengths at RT. The results reveal that the SNR increases

gradually with increasing wavelengths. The resonant effect in the cavity leads to an enhanced light-matter interaction in the active region of the device due to the high optical confinement factor and high reflectivity caused by the bottom DBR. As a result, the photogenerated current enhances and thus the output signal power. In addition, the SNR increases with wavelengths is due to more photo-generated carriers formed by per watt incident light. For longer wavelengths, each photon owns smaller energy. Hence, the light of $0.5 \mu\text{W}$ would be composed of more photons for longer wavelengths. The more photons can contribute to the more photo-generated electron-hole pairs. A higher photo-generated current source can then be achieved. Therefore, with increasing incident light wavelengths, the SNR increases at the output of PDs. Furthermore, the estimated results also suggest that the magnitude of SNR is less dependent on the frequency (f) up to 10^4 GHz, however, it decreases precipitately beyond $f > 10^4$ GHz. With the increase in operating frequency ($10 \text{ GHz} < f < 10^6 \text{ GHz}$), the SNR decreases by $\sim 7.2\%$ at 1550 nm . This decrease in SNR is due to the RC effect.

Most importantly, the computed SNR at the output of the proposed device can exceed 120 dB for the frequency range up to 10^4 GHz, which is significantly higher than the typical value of SNR ($\sim 60 \text{ dB}$)⁴⁶ for practical SWIR applications. These results prove that the designed device can be a potential detector for low noise and high-speed applications.

Conclusion

To reduce the *trade-off* between the responsivity and 3dB bandwidth and to get the high-performance, we investigated Si/SiO₂ DBR-integrated lateral Ge *p-i-n* PDs on Si substrate. In addition, π -model small-signal noise equivalent circuit modeling of the designed device was also proposed to compute the noise components and the SNR. The device exhibits the lowest dark current of $\sim 0.54 \text{ pA}$ at RT for $W = 4000 \text{ nm}$ compared to other Ge PDs and a photogenerated current-to-dark current ratio of $\sim 6.1 \times 10^5$, proving that the Ge-based films are highly photosensitive. The analysis showed that the spectral responsivity is strongly dependent on the aspect ratio (width to height). Moreover, the SNR of the device was significantly dependent on the operating frequency but less dependent on the incident light wavelength. For the optimal rib waveguide width and height, the device achieved excellent photosensitive characteristics such as high detectivity ($\sim 2.4 \times 10^{11}$ Jones at 1550 nm for $V = -2\text{V}$), high 3dB bandwidth (26.4 GHz for atmospheric gas sensing and 6.6 GHz for fiber-optic telecommunication networks), and extremely high SNR (120 dB up to 3 THz). Based on these encouraging results, we can conclude that the proposed device and its noise equivalent circuit model can achieve high-performance in the SWIR regime for atmospheric gas sensing applications and fiber-optic telecommunication networks.

Acknowledgements (optional)

This work was supported by the Ministry of Science and Technology, R.O.C., under contract No. MOST 110-2221-E-259-013. H Kumar and AKP would like to thank Dr. Rikmantra Basu (Assistant Professor) at Electronics and Communication Engineering, National Institute of Technology Delhi, New Delhi, India, and Dam Nonguk (Assistant Professor) at the Nanyang Technological University, Singapore for meaningful discussions. H Kumar would also like to thank Prof. and Head R Tomar, Research Prof. R. Gangopadhyay, and Prof. R Banerjee, Director, LNMIIT Jaipur, for their encouragement and support to undertake this work.

Author contributions

Conceptualization H.K.; methodology, H.K.; software, H.K. and A.K.P.; data curation, H.K., A.K.P.; writing—original draft preparation, H.K.; writing—review and editing, H.K., A.K.P. and C.H.L.; Supervision, C.H.L.; All authors have reviewed and agreed to the published version of the manuscript

References

1. Hu, W. *et al.* Germanium/perovskite heterostructure for high-performance and broadband photodetector from visible to infrared telecommunication band. *Light Sci. Appl.* **8**, 1–10 (2019).
2. Amoosoltani, N., Zarifkar, A. & Farmani, A. Particle swarm optimization and finite-difference time-domain (PSO/FDTD) algorithms for a surface plasmon resonance-based gas sensor. *J. Comput. Electron.* **18**, 1354–1364 (2019).
3. Shi, Y. *et al.* A silicon-based PbSe quantum dot near-infrared photodetector with spectral selectivity. *Nanoscale* **13**, 12306–12313 (2021).
4. Baqir, M. A. *et al.* Nanoscale, tunable, and highly sensitive biosensor utilizing hyperbolic metamaterials in the near-infrared range. *Appl. Opt.* **57**, 9447–9454 (2018).
5. Sargent, E. H. Solar cells, photodetectors, and optical sources from infrared colloidal quantum dots. *Adv. Mater.* **20**, 3958–3964 (2008).
6. Xu, H. *et al.* Flexible Organic/Inorganic Hybrid Near-Infrared Photoplethysmogram Sensor for Cardiovascular Monitoring. *Adv. Mater.* **29**, 1–6 (2017).
7. Park, S. *et al.* Ultraflexible near-infrared organic photodetectors for conformal photoplethysmogram sensors. *Adv. Mater.* **30**, 1–8 (2018).

8. Rogalski, A., Antoszewski, J. & Faraone, L. Third-generation infrared photodetector arrays. *J. Appl. Phys.* **105**, (2009).
9. He, J. *et al.* Synergetic Effect of Silver Nanocrystals Applied in PbS Colloidal Quantum Dots for High-Performance Infrared Photodetectors. *ACS Photonics* **1**, 936–943 (2014).
10. Cohen, M. J., Ettenberg, M. H., Lange, M. J. & Olsen, G. H. Commercial and industrial applications of indium gallium arsenide near-infrared focal plane arrays. in *Infrared Technology and Applications XXV* vol. 3698 453–461 (1999).
11. Kidder, L. H., Levin, I. W., Lewis, E. N., Kleiman, V. D. & Heilweil, E. J. Mercury cadmium telluride focal-plane array detection for mid-infrared Fourier-transform spectroscopic imaging. *Opt. Lett.* **22**, 742–744 (1997).
12. Wu, E. *et al.* In Situ Fabrication of 2D WS₂/Si Type-II Heterojunction for Self-Powered Broadband Photodetector with Response up to Mid-Infrared. *ACS Photonics* **6**, 565–572 (2019).
13. Chaisakul, P. *et al.* Recent progress on Ge/SiGe quantum well optical modulators, detectors, and emitters for optical interconnects. *Photonics* vol. 6 1–18 (2019).
14. Hu, T. *et al.* Silicon photonic platforms for mid-infrared applications [Invited]. *Photonics Res.* **5**, 417–430 (2017).
15. Michel, J., Liu, J. & Kimerling, L. C. High-performance Ge-on-Si photodetectors. *Nat. Photonics* **4**, 527–534 (2010).
16. Sorianello, V., De Iacovo, A., Colace, L. & Assanto, G. Near-infrared photodetectors in evaporated ge: Characterization and TCAD simulations. *IEEE Trans. Electron Devices* **60**, 1995–2000 (2013).
17. Dushaq, G., Nayfeh, A. & Rasras, M. Germanium metal-semiconductor-metal photodetectors grown on Silicon using low temperature RF-PECVD. *Opt. Express* **25**, 32110–32119 (2017).
18. Zang, H. *et al.* Dark-current suppression in metal-germanium-metal photodetectors through dopant-segregation in NiGe - Schottky barrier. *IEEE Electron Device Lett.* **29**, 161–164 (2008).
19. Asar, T. & Özçelik, S. Barrier enhancement of Ge MSM IR photodetector with Ge layer optimization. *Superlattices Microstruct.* **88**, 685–694 (2015).
20. Cervantes-González, J. C. *et al.* Germanium metal-semiconductor-metal photodetectors evanescently coupled with upper-level silicon oxynitride dielectric waveguides. *Appl. Phys. Lett.* **101**, 2012–2015 (2012).
21. Augel, L., Schlupf, J., Bullert, S., Bürzele, S., Schulze, J. & Fischer, I. A. Photonic-plasmonic mode coupling in nanopillar Ge-on-Si PIN photodiodes. *Sci. Rep.* **11**, 5723 (2021).
22. Benedikovic, D. *et al.* Comprehensive Study on Chip-Integrated Germanium Pin Photodetectors for Energy-Efficient Silicon Interconnects. *IEEE J. Quantum Electron.* **56**, 1–9 (2020).
23. Lin, Y. *et al.* High-efficiency normal-incidence vertical p-i-n photodetectors on a germanium-on-insulator platform. *Photonics Res.* **5**, 702–709 (2017).
24. Wang, L. *et al.* Infrared broadband enhancement of responsivity in Ge photodetectors decorated with Au nanoparticles. *Opt. Express* **29**, 12941–12949 (2021).
25. Zhao, X. *et al.* High performance p-i-n photodetectors on ge-on-insulator platform. *Nanomaterials* **11**, 1–11 (2021).
26. Cheng, C.-Y. *et al.* Ge-on-insulator lateral p-i-n waveguide photodetectors for optical communication. *Opt. Lett.* **45**, 6683–6686 (2020).
27. Kang, J., Takenaka, M. & Takagi, S. Ge photodetector monolithically integrated with amorphous Si waveguide on wafer-bonded Ge-on-insulator substrate. *Opt. Express* **26**, 30546–30555 (2018).
28. Assefa, S. *et al.* CMOS-integrated high-speed MSM germanium waveguide photodetector. *Opt. Express* **18**, 4986–4999 (2010).
29. Virost, L. *et al.* Integrated waveguide PIN photodiodes exploiting lateral Si/Ge/Si heterojunction. *Opt. Express* **25**, 19487–19496 (2017).
30. Balram, K. C., Audet, R. M. & Miller, D. A. B. Nanoscale resonant-cavity-enhanced germanium photodetectors with lithographically defined spectral response for improved performance at telecommunications wavelengths. *Opt. Express* **21**, 10228–10233 (2013).
31. Koester, S. J., Member, S., Schaub, J. D., Dehlinger, G. & Chu, J. O. Germanium-on-SOI Infrared Detectors for Integrated Photonic Applications. *IEEE J. Sel. Top. Quantum Electron.* **12**, 1489–1502 (2006).
32. Ghosh, S. *et al.* Resonant-cavity-enhanced responsivity in germanium-on-insulator photodetectors. *Opt. Express* **28**, 23739–23747 (2020).
33. Wang, J. & Lee, S. Ge-photodetectors for Si-based optoelectronic integration. *Sensors* **11**, 696–718 (2011).
34. Li, C. *et al.* High-responsivity vertical-illumination Si/Ge uni-traveling-carrier photodiodes based on silicon-on-insulator substrate. *Sci. Rep.* **6**, 1–9 (2016).
35. Li, C. *et al.* High performance silicon waveguide germanium photodetector. *Chinese Phys. B* **24**, 08502(1-5) (2015).
36. Li, C. *et al.* Effects of Interface States on Ge-On-SOI Photodiodes. *IEEE J. Electron Devices Soc.* **7**, 7–12 (2019).
37. Cho, M. *et al.* Amorphous Si/SiO₂ distributed Bragg reflectors with transfer printed single-crystalline Si nanomembranes. *J. Vac. Sci. Technol. B, Nanotechnol. Microelectron. Mater. Process. Meas. Phenom.* **34**, 040601 (2016).
38. Soref, R. A., Schmidtchen, J. & Petermann, K. Large Single-Mode Rib Waveguides in GeSi-Si and Si-on-SiO₂. *IEEE J. Quantum Electron.* **27**, 1971–1974 (1991).
39. Benedikovic, D. *et al.* Silicon – germanium receivers for short-wave- infrared optoelectronics and communications. *Nanophotonics* **10**, 1059–1079 (2020).
40. Zhou, H. *et al.* High-efficiency GeSn/Ge multiple-quantum-well photodetectors with photon-trapping microstructures operating at 2 μm. *Opt. Express* **28**, 10280–10293 (2020).
41. Chang, G. E., Basu, R., Mukhopadhyay, B. & Basu, P. K. Design and Modeling of GeSn-Based Heterojunction Phototransistors for Communication Applications. *IEEE J. Sel. Top. Quantum Electron.* **22**, 8200409(1–9) (2016).
42. Deen, M. J. & Basu, P. K. *Silicon Photonics: Fundamentals and Devices*. (John Wiley & Sons, 2012).
43. Lin, Y., Lee, K. H., Son, B. & Tan, C. S. Low-power and high-detectivity Ge photodiodes by in-situ heavy As doping during Ge-on-Si seed layer growth. *Opt. Express* **29**, 2940–2952 (2021).
44. Lee, B. H. *et al.* Highly responsive near-infrared photodetector with low dark current using graphene/germanium Schottky junction with Al₂O₃ interfacial layer. *Nanophotonics* **10**, 1573–1579 (2021).
45. Conley, B. R. *et al.* Si based GeSn photoconductors with a 1.63 A/W peak responsivity and a 2.4 μm long-wavelength cutoff. *Appl. Phys. Lett.* **105**, 221117(1–5) (2014).
46. Pandey, A. K., Basu, R., Kumar, H. & Chang, G. E. Comprehensive Analysis and Optimal Design of Ge/GeSn/Ge p-n-p Infrared Heterojunction Phototransistors. *IEEE J. Electron Devices Soc.* **7**, 118–126 (2019).